



# Martensitic microstructures and mechanical properties of as-quenched metastable $\beta$ -type Ti–Mo alloys

C. H. Wang<sup>1</sup>, C. D. Yang<sup>1</sup>, M. Liu<sup>1</sup>, X. Li<sup>1</sup>, P. F. Hu<sup>2</sup>, A. M. Russell<sup>3</sup>, and G. H. Cao<sup>1,\*</sup>

<sup>1</sup>State Key Laboratory of Advanced Special Steel and Shanghai Key Laboratory of Advanced Ferrometallurgy and School of Materials Science and Engineering, Shanghai University, 149 Yanchang Road, Shanghai 200072, People's Republic of China

<sup>2</sup>Laboratory for Microstructures, Shanghai University, 99 Shangda Road, Shanghai 200444, People's Republic of China

<sup>3</sup>Division of Materials Science and Engineering Ames Laboratory of the U.S.D.O.E., Department of Materials Science and Engineering, Iowa State University, Ames, IA 50011-2300, USA

Received: 30 December 2015

Accepted: 11 April 2016

Published online:

21 April 2016

© Springer Science+Business Media New York 2016

## ABSTRACT

Microstructures and tensile properties were investigated in metastable  $\beta$ -type Ti–10Mo, Ti–15Mo, and Ti–20Mo alloys after solution treatment. In addition to  $\beta$  phase, different martensitic structures with various sizes and morphologies were found in these alloys. In the Ti–10Mo alloy, acicular  $\alpha''$  plates were uniformly distributed in the  $\beta$  matrix. Transmission electron microscopy (TEM) revealed  $\{111\}$   $\alpha''$ -type twins had formed in  $\alpha''$  plates, and the orientation relationship between the  $\beta$  and  $\alpha''$  is close to  $(110) \beta // (001) \alpha''$ ,  $(1\bar{1}2) \beta // (110) \alpha''$ , and  $[\bar{1}11] \beta // [\bar{1}10] \alpha''$ . In the Ti–15Mo alloy, nanoparticles of athermal  $\omega$  phase containing  $\{112\}$   $\beta$ -type twins were observed in the  $\beta$  matrix. Smaller  $\omega$  particles were found in the Ti–20Mo alloy than in the Ti–15Mo alloy. When tensile tested, the Ti–10Mo and Ti–15Mo alloys exhibited large plastic strains of 24 and 29 %, respectively, with ultimate tensile stresses of 756 and 739 MPa. The Ti–20Mo alloy displayed a higher ultimate tensile stress of 792 MPa but much smaller plastic strain (2 %). Although  $\beta$  phase dominates in all the metastable  $\beta$ -type Ti–Mo alloys, the nanostructured martensites also play an important role in the mechanical properties of the alloys.

## Introduction

Titanium and its alloys have attracted considerable attention for biomedical applications due to their low specific gravity, high corrosion resistance, low elastic moduli, and superior biocompatibility [1–3]. Presently,  $\alpha$ -type commercially pure titanium (CP Ti) and  $\alpha + \beta$  type Ti–6Al–4V are the most frequently

used implant materials, but some studies show that the release of both V and Al ions from Ti–6Al–4V might induce some long-term health problems [4–6]. In addition, its relatively high Young's modulus ( $\sim 110$  GPa) compared to bone tissue (10–40 GPa) could cause a stress-shielding effect, which is deleterious to the patient.

Address correspondence to E-mail: ghcao@shu.edu.cn

More recently, much research effort has been devoted to the study of  $\beta$  and metastable  $\beta$ -Ti alloys with lower moduli, better formability, and higher biocompatibility than  $\alpha$  and  $\alpha + \beta$  Ti alloys, and a series of metastable  $\beta$  titanium alloys for biomedical applications has been developed that includes Ti–15Mo, Ti–12Mo–6Zr–2Fe (TMZF), and Ti–35Nb–7Zr–5Ta (TNZT) [7, 8]. Among these alloys, Ti–Mo and Ti–Mo-based alloys have received much attention because of the remarkable  $\beta$ -stabilizing effect and the favorable safety of Mo [2, 9]. Furthermore, based on the stress-induced  $\beta$ -to- $\alpha'$  martensitic transformation of Ti–Mo-based alloys [9–11], they have also been developed as Ni-free superelastic and shape memory Ti alloys that could replace Ti–Ni, which has been suspected of producing allergenic and carcinogenic reactions from its Ni content [12, 13].

Realizing the promising biomedical applications of Ti–Mo and Ti–Mo-based alloys described above, extensive fundamental research has been carried out on the microstructure and mechanical properties of binary Ti–Mo alloys. Ho et al. [14] studied the structure of a series of cast binary Ti–Mo alloys and found that martensitic phases were formed in alloys containing  $\leq 10$  wt% Mo, and the retained  $\beta$  phase became the only dominant phase when Mo content exceeds 10 wt%. Zhao et al. [15] reported that the Ti–15Mo and Ti–16Mo alloys subjected to solution treatment comprised a  $\beta$  phase and a certain amount of athermal  $\omega$  phase, whereas the Ti–17Mo and Ti–18Mo alloys under the same condition consisted of a single  $\beta$  phase. On the other hand, Sabeena et al. [16] studied the microstructures of martensite in Ti–Mo alloys quenched from the high-temperature  $\beta$ -phase field and discovered that  $\alpha'$  martensite coexisted with  $\beta$  and  $\omega$  phase in the Ti–15Mo and Ti–25Mo alloys. Therefore, there is still no clear consensus concerning the martensitic structures and phase constitution of solution-treated metastable  $\beta$ -type Ti–Mo alloys. Because superior mechanical properties with a good combination of strength and ductility are required in biomedical applications, a better understanding of microstructure–mechanical property relationships is important for these alloys. Hanada et al. [17, 18] reported that the tensile properties of  $\beta$ -Ti alloys were strongly influenced by deformation modes that depended on the stability of  $\beta$  phase. Marteleur and Sun et al. [19, 20] utilized the d-electron alloy design strategy to elucidate the mechanical properties of  $\beta$ -Ti alloys by connecting two electronic

parameters to the chemical stability of the  $\beta$  phase and experimentally validated that the Ti–12Mo alloy exhibited high ductility induced by mechanical twinning and stress-induced martensitic transformation. However, in addition to the stability of the  $\beta$  phase, the effect of martensites on the mechanical properties of metastable  $\beta$ -Ti alloys should also be taken into consideration.

In the present study, the microstructural characteristics and mechanical properties were investigated in Ti–10Mo, Ti–15Mo, and Ti–20Mo binary alloys. This research focused particularly on the morphologies and microstructures of martensites and their effect on the mechanical properties of these alloys.

## Materials and methods

Three metastable  $\beta$ -type Ti–Mo alloys, containing 10, 15, and 20 wt% molybdenum were fabricated by cold crucible levitation melting of Ti and Mo metals of 99.99 % purity (supplied by China New Metal Materials Technology Co., Ltd). Melting was performed under an Ar atmosphere in a water-cooled Cu crucible. The ingots were turned over and remelted four times to ensure homogeneous compositions. The cast alloys were sealed in quartz capsules evacuated to a pressure of about  $1 \times 10^{-5}$  Pa, and solution treated at 1000 °C for  $3.6 \times 10^3$  s. After solution treatment, the alloys were quenched by breaking the capsules in iced water. The phase constitutions of as-quenched alloys were determined by a D/MAX-3C X-ray diffractometer (XRD) using Cu  $K\alpha_1$  radiation ( $\lambda = 0.1541$  nm) in the range  $2\theta = 20$ – $100^\circ$  with a step size of  $0.02^\circ$  and a counting time of 1 s per step. Specimens for optical microscope (OM) observation were cut by electrical-discharge machining (EDM) from as-quenched alloys, then mechanically polished via a standard metallographic procedure to a final level of 1  $\mu\text{m}$  diamond powder and etched in a solution composed of 5 vol% HF, 10 vol% HNO<sub>3</sub>, and 85 vol% H<sub>2</sub>O. The microstructure of the etched specimens was examined by an OM (DM 6000 M, LEICA). Disks of about 0.2 mm in thickness were cut from as-quenched alloys for TEM specimens by EDM. The disks were mechanically ground to a thickness of  $\sim 80$   $\mu\text{m}$ . Electron-transparent foils were prepared by jet electropolishing using an electrolyte consisting of 65 vol% methanol, 30 vol% butanol, and 5 vol% perchloric acid at a

voltage of 30 V and temperatures between  $-30$  and  $-40$  °C. The thin foils were then examined using a JEOL 2010F transmission electron microscope equipped with a field emission gun operated at an acceleration voltage of 200 kV. Tensile specimens with a gage size of  $3 \times 1.5 \times 14$  mm were cut from as-quenched alloys by EDM. The tensile tests were performed using a MTS C40 electronic universal testing machine with an Epsilon 3442 electronic extensometer at ambient temperature with an initial strain rate of  $2 \times 10^{-4} \text{ s}^{-1}$ . The average tensile test data given in this paper were taken from three tensile experiments for each alloy. The fracture surfaces were characterized by a JSM-7001 scanning electron microscope (SEM).

## Results

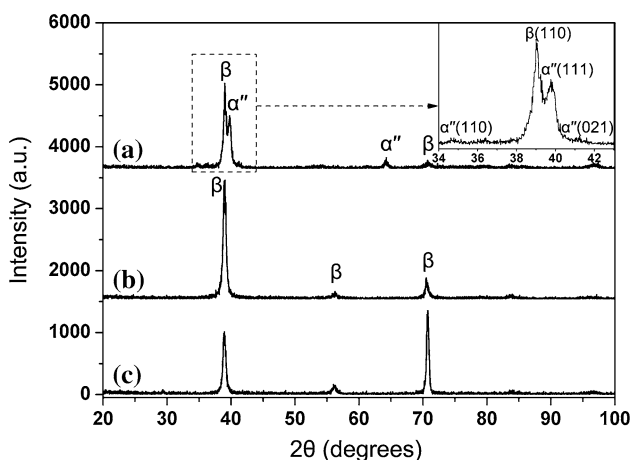
### Microstructure of as-quenched Ti–Mo alloys

The XRD diffractograms of the as-quenched Ti–Mo alloys are shown in Fig. 1. It can be seen that  $\beta$  phase is the dominant phase in all the Ti–Mo alloys. Some peaks deviating from  $\beta$ -phase reflections were observed in Fig. 1a. Analysis of these peaks indicated the presence of orthorhombic  $\alpha''$  phase in the Ti–10Mo alloy as shown in the partial enlarged view of Fig. 1a. Only  $\beta$  phase was detected in the Ti–15Mo alloy (Fig. 1b) and Ti–20Mo alloy (Fig. 1c). From the strongest (110)  $\beta$  peaks, one can calculate the lattice parameter of  $\beta$  phase,  $a = 0.326$  nm for the Ti–10Mo

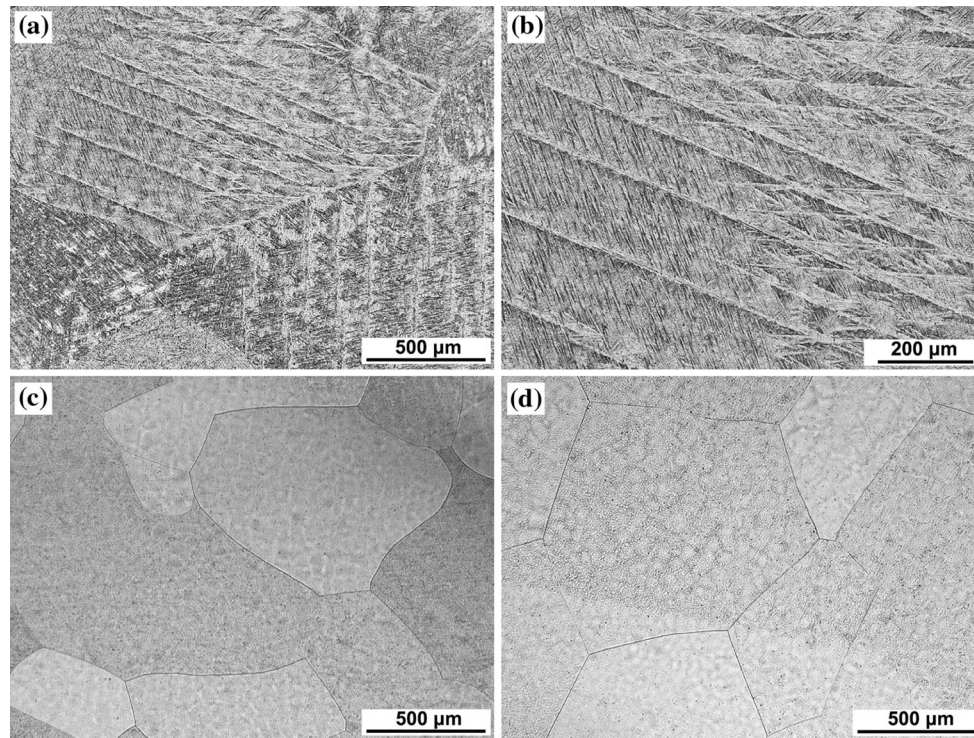
alloy,  $a = 0.327$  nm for the Ti–15Mo alloy, and  $a = 0.327$  nm for the Ti–20Mo alloy. Some earlier investigators pointed out the presence of  $\omega$  phase in the Ti–10 to 20Mo alloys [15, 16], but  $\omega$  phase is difficult to detect by XRD since  $\beta$  and  $\omega$  phase peaks overlap [20–22]. Therefore, TEM is necessary for the determination of  $\alpha''$  and  $\omega$  phases.

Figure 2 shows the typical optical micrographs of as-quenched Ti–Mo alloys. The microstructures are consistent with the XRD results. As shown in Fig. 2a, the Ti–10Mo alloy exhibits a fine, acicular martensitic structure (identified as  $\alpha''$  phase by XRD) distributed homogeneously over the large grains of the  $\beta$  matrix. A higher magnification image of the  $\alpha''$  plates is shown in Fig. 2b. It is noted that  $\alpha''$  martensite plates start from  $\beta$  grain boundaries and end in the interior of  $\beta$  grains, implying that the  $\alpha''$  martensite nucleates on  $\beta$  grain boundaries and grows into the interior of  $\beta$  grains during quenching. In Fig. 2c, d only equiaxed  $\beta$  grains with an average grain size of about  $500 \mu\text{m}$  were observed, indicating that no martensites can be detected by optical microscopy in the Ti–15Mo and Ti–20Mo alloys.

In order to characterize the microstructure and phase constitution in detail, TEM investigation was carried out on the as-quenched metastable  $\beta$ -type Ti–Mo alloys. The TEM images and corresponding selected area electron diffraction (SAED) patterns obtained from the Ti–10Mo alloy are shown in Fig. 3. Figure 3a, b are two complementary dark-field images that show  $\alpha''$  plates with or without substructures in the Ti–10Mo alloy. Figure 3c shows the corresponding SAED patterns from which Fig. 3a, b were obtained by using two twin-related spots (indicated by two circles in Fig. 3c). Figure 3c reveals that the substructures in  $\alpha''$  plates are twins and indicates the  $\{111\}$   $\alpha''$ -type twin relationship of adjacent  $\alpha''$  plates and internal twins. Figure 3d–i presents another typical region containing both  $\alpha''$  plates and  $\beta$  matrix that were investigated to identify the crystallographic relationship between the  $\beta$  and  $\alpha''$  phase. Figure 3d displays the dark-field image acquired by using the circled reflections corresponding to  $\beta$  matrix and one  $\alpha''$  twin lamella in Fig. 3e and shows the morphology of the  $\beta$  grain and  $\alpha''$  twin lamellae, which are distributed at intervals. The SAED patterns in Fig. 3e were taken from the selected region denoted by the white circle in the corresponding bright-field image (Fig. 3g) and can be indexed as the  $[\bar{1}11]$  zone axis



**Figure 1** XRD diffractograms of *a* Ti–10Mo, *b* Ti–15Mo, and *c* Ti–20Mo alloys.



**Figure 2** Optical micrographs of **a, b** Ti–10Mo, **c** Ti–15Mo, and **d** Ti–20Mo alloys.

pattern of the  $\beta$  matrix superimposed with the  $[\bar{1}10]$  zone axis pattern of  $\alpha''$  martensite. Figure 3f is the key diagram of Fig. 3e. The analyses of diffraction patterns in Fig. 3e reveal that the orientation relationship between the  $\beta$  parent matrix and  $\alpha''$  phase is close to  $(110) \beta // (001) \alpha''$ ,  $(1\bar{1}2) \beta // (110) \alpha''$ , and  $[\bar{1}11] \beta // [\bar{1}10] \alpha''$ . The corresponding SAED patterns in Fig. 3h are taken from the region including the  $\beta$  matrix and multiple  $\alpha''$  lamellae (marked by the black circle in Fig. 3g). In reference to Fig. 3e, the composite patterns in Fig. 3h can be indexed as the  $[\bar{1}11]$  zone axis pattern of the  $\beta$  phase superimposed with the  $[\bar{1}10]$  zone axis pattern of  $\{111\} \alpha''$ -type twinned  $\alpha''$  plates as depicted in the key diagram (Fig. 3i). This confirms that  $\alpha''$  plates with  $\{111\} \alpha''$ -type internal twins are homogeneously distributed in the  $\beta$  matrix. The lattice parameters of  $\alpha''$  phase measured by corresponding SAED patterns were determined to be  $a = 0.307$  nm,  $b = 0.493$  nm, and  $c = 0.466$  nm.

The TEM images and corresponding SAED patterns obtained from the Ti–15Mo alloy are given in Fig. 4. Figure 4a shows the  $\beta$   $[110]$  zone axis diffraction pattern with the addition of superlattice spots at various  $1/3 \langle 112 \rangle \beta$  and  $2/3 \langle 112 \rangle \beta$  positions as a result

of the coexistence of  $\omega$  and  $\beta$  phase [23–25]. The corresponding dark-field image in Fig. 4b was taken using a spot of  $\omega$  phase, as indicated by a circle in Fig. 4a. Figure 4a, b confirms the presence of athermal  $\omega$  phase in the Ti–15Mo alloy, and the lattice parameters of  $\omega$  phase were measured to be  $a = 0.462$  nm and  $c = 0.283$  nm. The  $\omega$  phase was formed as fine particles (less than 10 nm) that were uniformly dispersed in the  $\beta$  matrix. Some fine parallel laths with a width of about 10 nm were observed in the  $\beta$  matrix. Figure 4c, d shows the SAED patterns and corresponding dark-field image of the laths, respectively. The dark-field image in Fig. 4d was formed using the overlapped reflections denoted by the circle in Fig. 4c. Analysis of the SAED patterns indicates that the laths are  $\{112\} \beta$ -type twins. Figure 4c can be indexed as the SAED patterns of  $\beta$  matrix containing athermal  $\omega$  phase (Fig. 4a) superimposed on its twin-related spots, as illustrated in Fig. 4e.

The TEM images and corresponding SAED patterns obtained from the Ti–20Mo alloy are presented in Fig. 5. As shown in Fig. 5a, no martensitic structures were observed in the  $\beta$  matrix in the Ti–20Mo alloy. The SAED pattern of the  $[\bar{1}13]$  zone axis of  $\beta$

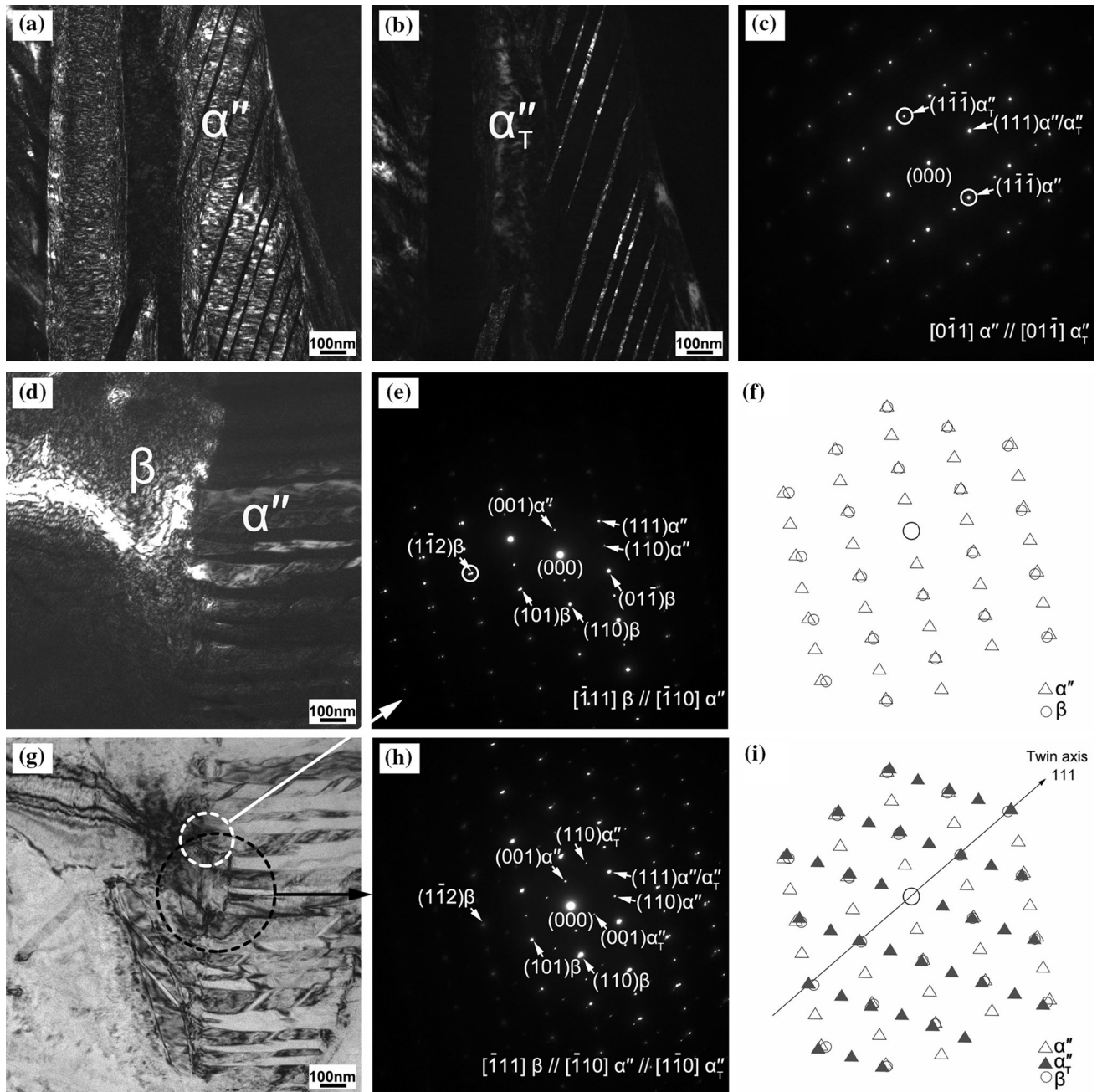


**Figure 3** TEM dark-field images **a**, **b** showing  $\alpha''$  plates and internal twins, **c** SAED patterns of  $\alpha''$  plates along  $[01\bar{1}]$  zone axis, **d** dark-field images of  $\alpha''$  plates and  $\beta$  matrix in Ti–10Mo alloy, **e** SAED patterns of  $\alpha''$  plates and  $\beta$  phase along  $[\bar{1}10]$  and  $[\bar{1}11]$

zone axes, **f** key diagram of **e**, **g** bright-field images of  $\alpha''$  twinned plates and  $\beta$  matrix, **h** SAED patterns of  $\alpha''$  twinned plates and  $\beta$  phase along  $[\bar{1}10]$ , and  $[\bar{1}11]$  zone axes, **i** key diagram of **h**.

phase (Fig. 5b) shows extra diffuse streaks at various  $1/3 \langle 112 \rangle \beta$  and  $2/3 \langle 112 \rangle \beta$  positions, suggesting that athermal  $\omega$  phase was also formed in the Ti–20Mo alloy. The dark-field image in Fig. 5c taken

from the  $\omega$  reflections (labeled by the circle in Fig. 5b) shows the appearance of extremely fine  $\omega$  particles that are smaller than the  $\omega$  particles in the Ti–15Mo alloy.

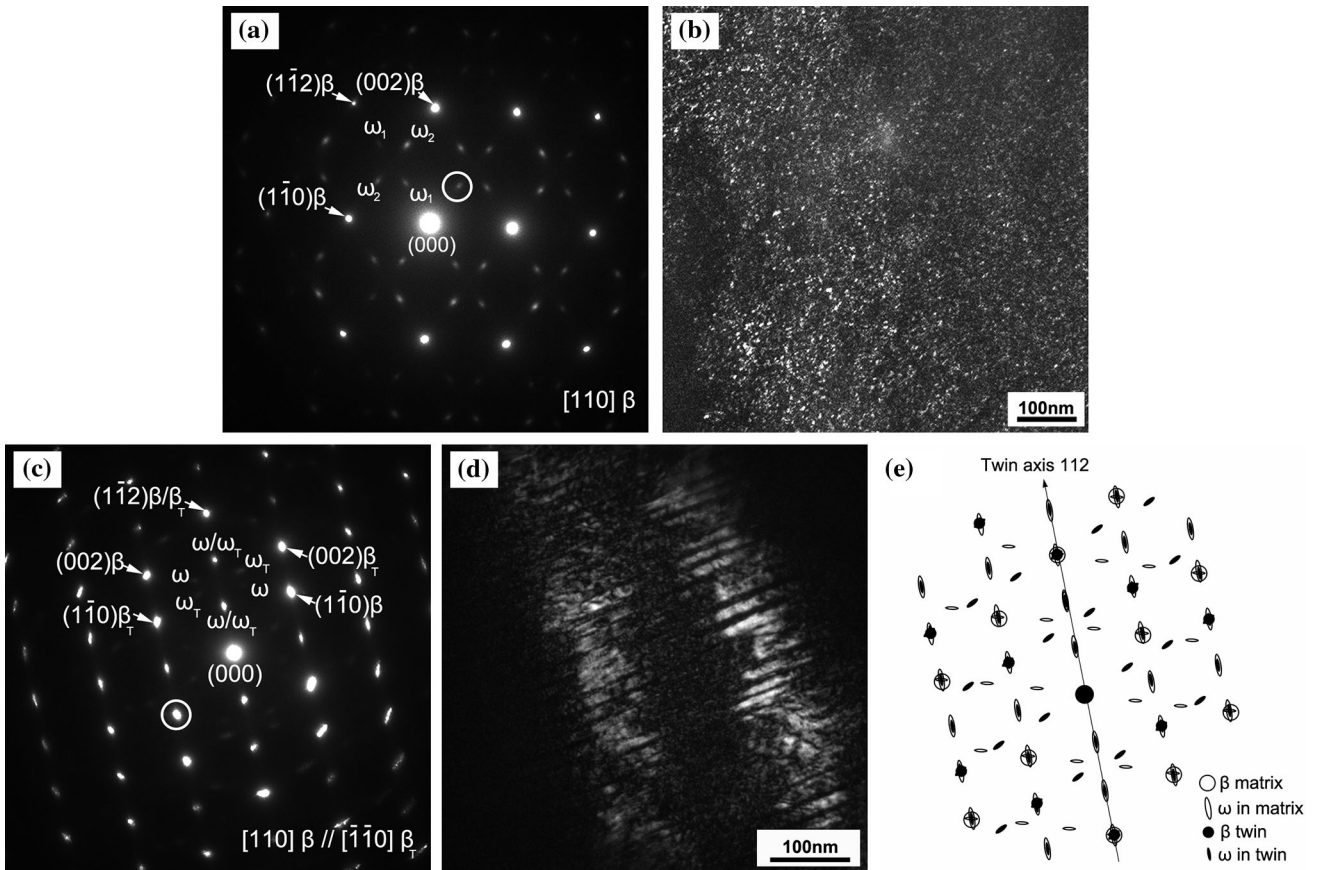


**Figure 4** a SAED pattern of  $\omega$  phase and  $\beta$  phase along  $[110]$  zone axis in Ti-15Mo alloy, b dark-field image of  $\omega$  phase, c SAED pattern of  $\omega$  phase and twinned  $\beta$  phase along  $[110]$  zone axis, d dark-field image of twinned  $\beta$  phase and  $\omega$  phase, and e key diagram of c.

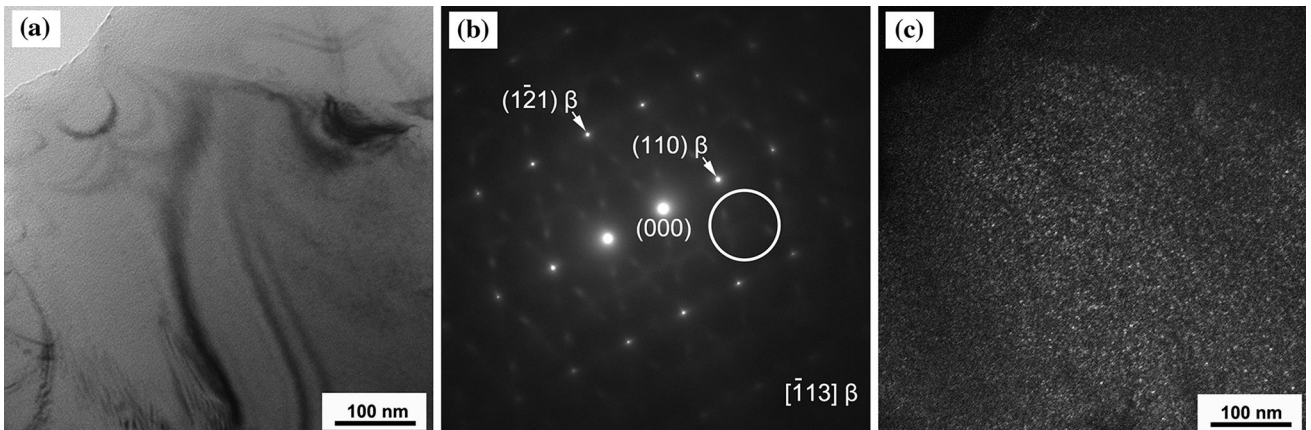


**Figure 5** a TEM bright-field image of  $\beta$  phase in Ti-20Mo alloy, b SAED pattern of  $\beta$  phase along  $[\bar{1}13]$  zone axis, c dark-field image of  $\omega$  phase.

### Mechanical properties of as-quenched Ti-Mo alloys

Figure 6 shows stress–strain curves from the Ti-Mo alloys’ room-temperature tensile tests. The tensile test

data for these Ti-Mo alloys are presented in Table 1. The Ti-10Mo and Ti-15Mo alloys display yield stresses of 420 and 302 MPa, followed by extensive work hardening, resulting in large plastic strains of 24 and 29 %, respectively. In contrast, the Ti-20Mo

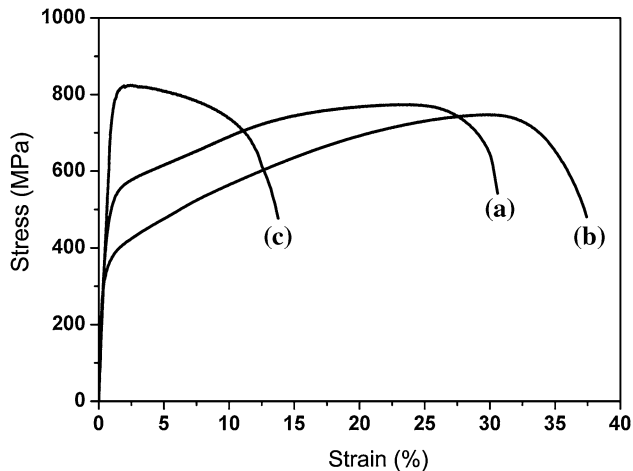


**Figure 6** Typical tensile stress–strain curves of *a* Ti–10Mo, *b* Ti–15Mo, and *c* Ti–20Mo alloys.

**Table 1** Tensile test data of the Ti–Mo alloys

Alloys	$E$ (GPa)	$\sigma_y$ (MPa)	$\sigma_{max}$ (MPa)	$\varepsilon_p$ (%)
Ti–10Mo	$97 \pm 3$	$420 \pm 31$	$756 \pm 17$	$24 \pm 2$
Ti–15Mo	$104 \pm 6$	$302 \pm 18$	$739 \pm 38$	$29 \pm 2$
Ti–20Mo	$83 \pm 10$	$734 \pm 36$	$792 \pm 42$	$2 \pm 1$

$E$  Young's modulus,  $\sigma_y$  yield stress,  $\sigma_{max}$  ultimate tensile stress,  $\varepsilon_p$  plastic strain

alloy exhibits a yield strength of 734 MPa and low plastic strain of 2 % with far less work hardening than occurred in the Ti–10Mo and Ti–15Mo tensile tests. Although the Ti–10Mo and Ti–15Mo alloys show much lower yield stress, they display both high ultimate tensile strength and excellent ductility that would be desirable for biomedical applications.

The investigation of the fracture surfaces by SEM was performed on the Ti–Mo alloys after tensile testing. Secondary electron (SE) fractographs of the Ti–Mo alloys are shown in Fig. 7. It can be seen that all the fracture surfaces contain dimples with different sizes, implying that ductile fracture characteristics were present to varying degrees. The predominant fracture mode of the Ti–10Mo and Ti–15Mo alloys is microvoid coalescence, as presented in Fig. 7a, b. However, larger dimples formed in the fracture surface of the Ti–15Mo alloy, than those in the Ti–10Mo alloy, indicate that the Ti–15Mo alloy shows better ductility than the Ti–10Mo alloy, which is also evident from the tensile test plot (Fig. 6). In Fig. 7c, apart from small dimples, features of cleavage facets are more pronounced, which indicates that

the Ti–20Mo alloy displays some manifestations of both ductile failure and brittle fracture (cleavage fracture mode).

## Discussion

### Formation of the martensites during quenching

The above microstructural observations and analyses suggest the formation of  $\alpha''$  martensite in the Ti–10Mo alloy and athermal  $\omega$  martensite in the Ti–15Mo and Ti–20Mo alloys during quenching. As  $\alpha''$  martensitic transformation occurs, the [100]  $\beta$  direction shrinks to form [100]  $\alpha''$ , and the  $[\bar{1}10]$   $\beta$  direction expands to form [010]  $\alpha''$  [26]. Based on this mechanism, a schematic diagram illustrating the lattice correspondence between the  $\beta$  and  $\alpha''$  phase is given in Fig. 8. The orientation relationship between the  $\beta$  and  $\alpha''$  phase determined in this study is equivalent to those proposed by other researchers [13, 20, 27], and all of them conform with the lattice correspondence exhibited in Fig. 8. The athermal  $\omega$  phase has been frequently observed in metastable Ti alloys quenched from the high-temperature  $\beta$ -phase field [28–31]. It is reported that the  $\omega$  lattice is obtained by the collapse of one pair of (111)  $\beta$  planes to the intermediate position leaving the adjacent (111)  $\beta$  planes unaltered via a shuffle mechanism that follows these orientation relationships: (111)  $\beta$  // (0001)  $\omega$ ,  $[\bar{1}10]$   $\beta$  //  $[\bar{1}120]$   $\omega$  [32–34]. The TEM investigation of Ti-(18–22)V (wt%) alloys subjected to solution treatment revealed that the intensities of the  $\omega$  reflections in Ti–20V alloy were much weaker than those in Ti–18V alloy, and the  $\omega$  reflections in Ti–22V alloy disappeared, suggesting that the formation of athermal  $\omega$  phase becomes difficult as the stability of  $\beta$  phase increases [35]. Therefore, the change of the  $\omega$  reflections from sharp spots in the Ti–15Mo alloy (Fig. 4a) to weak and diffuse streaks in the Ti–20Mo alloy (Fig. 5b) could also arise from an increased resistance against the formation of  $\omega$  phase because of the increased stability of  $\beta$  phase and an incomplete (111) plane collapse from  $\beta$  phase during the martensitic transformation.

The substructure of martensites depends on the shear mode of martensitic transformation. At high phase-transition temperatures, shear by slip is easily motivated and causes a dislocated martensite, while

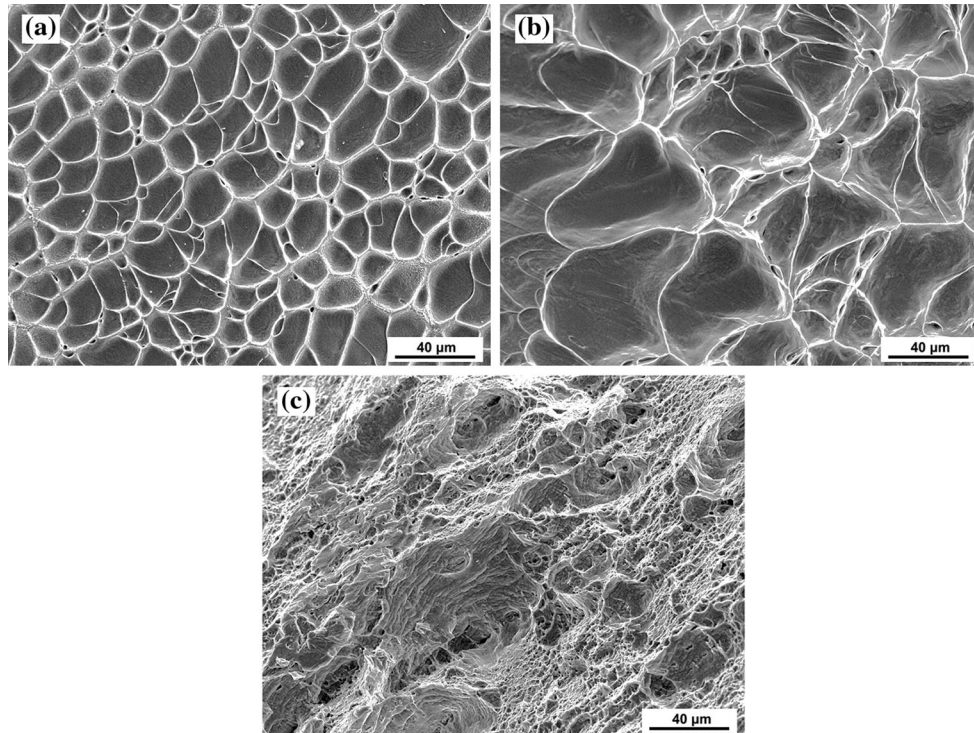


**Figure 7** SEM SE fractographs of **a** Ti–10Mo, **b** Ti–15Mo, and **c** Ti–20Mo alloys.

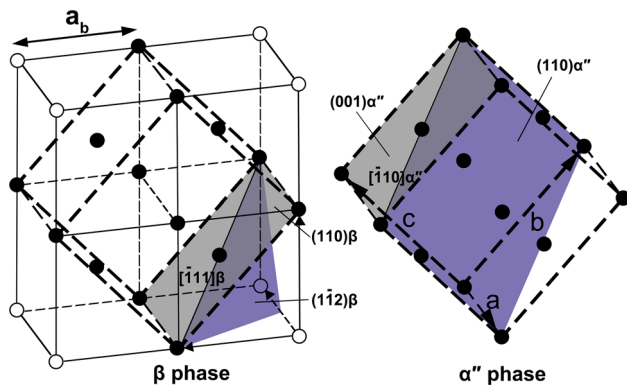


**Figure 8** A schematic illustrating the lattice correspondence between the  $\beta$  and  $\alpha''$  phases.

at low phase-transition temperatures, shear by twinning is easier to initiate and forms a twinned martensite. Meanwhile, the martensitic start temperature ( $M_s$ ) of  $\beta$ -isomorphous alloys decreases as the solute content increases [36, 37]. In this case, a transition of substructure from dislocations in  $\alpha'$  martensite of near  $\alpha$ -Ti alloys to twins in  $\alpha''$  martensite of metastable  $\beta$ -Ti alloys would be expected. Examination of dilute Ti–Mo alloys after quenching

confirmed that  $\alpha'$  plates contained a high density of dislocations and infrequent  $\{10\bar{1}1\}$  twins [38]. By comparison, the frequent observation of  $\{111\}$  twins in  $\alpha''$  plates in the Ti–10Mo alloy (Fig. 3) could be rationalized.

The  $\{112\}$   $\beta$ -type twins were frequently found in deformed  $\beta$ -Ti alloys [24, 39, 40], and were found to be one of the deformation mechanisms of metastable  $\beta$ -Ti alloys [20, 27]. However, the appearance of  $\{112\}$   $\beta$ -type twins in quenched Ti alloys was rarely reported. Recently, Wu et al. [41] investigated the  $\{112\}$   $\beta$ -type twins in Ti–30Nb–3Pd alloy processed by a solid-solution treatment at 900 °C for 1 h followed by furnace cooling to room temperature and proposed an  $\omega$ -lattice mechanism to explain the formation of  $\{112\}$   $\beta$ -type twins under no external stress or internal strain. The  $\{112\}$   $\beta$ -type twin was formed during the reverse transition of a metastable nanoscale  $\omega$  phase when the atoms attempted to return to the original matrix lattice but faced two identical choices. In this case, the appearance of  $\{112\}$   $\beta$ -type twins in the quenched Ti–15Mo alloy may be attributed to the reverse transformation ( $\omega \rightarrow \beta$ ) during the solution treatment.



## The effect of as-quenched microstructures on mechanical properties

It has been well established that the tensile properties of the metastable  $\beta$ -type Ti alloys depend significantly on the deformation mode with respect to the stability of the  $\beta$  phase. The deformation mode changes from twinning to slip as the stability of  $\beta$  phase increased, and consequently causes the yield strength increases and the elongation decreases with the increase of Mo content [17, 18, 42]. Thus, the Ti–20Mo alloy exhibits much higher yield strength and lower ductility than the Ti–10Mo and Ti–15Mo alloys. Moreover, the solid solution strengthening of  $\beta$  phase could also contribute to the higher strength in the Ti–20Mo alloy.

However, the mechanical properties of metastable  $\beta$ -type Ti alloys may be influenced by others factors, such as grain size, precipitation hardening, and the type of phases existing in the alloys. In this study, the coarser grain size exhibited in the Ti–10Mo alloy may have an adverse effect on its strength and ductility due to the Hall–Petch mechanism [5]. On the other hand, in association with the refinement effect of its twinned substructure, the  $\alpha''$  martensite formed in the Ti–10Mo alloy can improve the strength due to the higher stress needed for  $\alpha''$  phase to deform than  $\beta$  phase [43, 44], and ultimately induces a combination of high strength and good ductility in the Ti–10Mo alloy. The  $\omega$  phase is known as a harder phase than  $\alpha''$  or  $\beta$  phase, and a high density of fine  $\omega$  particles will strengthen the alloys [23]. However, the size of  $\omega$  particle is vital. Once the size of  $\omega$  particle becomes large enough, it may cause unexpected embrittlement [45]. Therefore, the extremely fine athermal  $\omega$  particles in the Ti–15Mo alloy, different from the isothermal  $\omega$  precipitation formed during aging, induce no visible brittleness in  $\beta$  phase. Furthermore, the pre-existent {112}  $\beta$  twins induced by  $\omega$  phase (Fig. 4c) also play an enhanced role in improving the ductility of the Ti–15Mo alloy [46]. In contrast, the  $\omega$  phase with a small size and less ideal structure makes it difficult to form {112}  $\beta$  twins in the Ti–20Mo alloy. Hence, the martensitic structure in the Ti–20Mo alloy does not improve ductility. In addition, because the  $\omega$  phase has higher elastic modulus than  $\alpha''$  and  $\beta$  phases [47], the Ti–15Mo alloy exhibits higher elastic modulus than the Ti–10Mo and Ti–20Mo alloys.

## Conclusions

All three metastable  $\beta$ -type Ti–Mo alloys contained fine martensitic structures distributed homogeneously in the  $\beta$  matrix after quenching. Acicular  $\alpha''$  plates with {111} twins, fine particles of athermal  $\omega$  phase, and {112}  $\beta$  twins were observed in the Ti–10Mo and Ti–15Mo alloys, respectively.  $\omega$  phase with smaller size appeared in the Ti–20Mo alloy. The Ti–10Mo and Ti–15Mo alloys show a good combination of extensive ductility and good strength, while the Ti–20Mo alloy exhibits higher yield strength and lower ductility. The formation of martensites becomes difficult as the stability of the  $\beta$  phase increases. The fine martensitic structures and twins enhance ductility in the Ti–10Mo and Ti–15Mo alloys.

## Acknowledgements

This work was supported by the National Natural Science Foundation of China (NSFC) under Grant 51271107. Support by the Instrumental Analysis and Research Center of Shanghai University are gratefully acknowledged.

## References

- [1] Li Q, Niinomi M, Hieda J, Nakai M, Cho K (2013) Deformation-induced omega phase in modified Ti–29Nb–13Ta–4.6Zr alloy by Cr addition. *Acta Biomater* 9:8027–8035
- [2] Niinomi M (2003) Recent research and development in titanium alloys for biomedical applications and healthcare goods. *Sci Technol Adv Mat* 4:445–454
- [3] Wang K (1996) The use of titanium for medical applications in the USA. *Mater Sci Eng A* 213:134–137
- [4] Long M, Rack HJ (1998) Titanium alloys in total joint replacement—a materials science perspective. *Biomaterials* 19:1621–1639
- [5] Lu JW, Zhao YQ, Ge P, Niu HZ (2013) Microstructure and beta grain growth behavior of Ti–Mo alloys solution treated. *Mater Charact* 84:105–111
- [6] Okazaki Y, Ito Y, Kyo K, Tateishi T (1996) Corrosion resistance and corrosion fatigue strength of new titanium alloys for medical implants without V and Al. *Mater Sci Eng A* 213:138–147
- [7] Banerjee R, Nag S, Stechschulte J, Fraser HL (2004) Strengthening mechanisms in Ti–Nb–Zr–Ta and Ti–Mo–Zr–Fe orthopaedic alloys. *Biomaterials* 25:3413–3419

- [8] Nag S, Banerjee R, Fraser HL (2005) Microstructural evolution and strengthening mechanisms in Ti–Nb–Zr–Ta, Ti–Mo–Zr–Fe and Ti–15Mo biocompatible alloys. *Mater Sci Eng C* 25:357–362
- [9] Zhou T, Aindow M, Alpay SP, Blackburn MJ, Wu MH (2004) Pseudo-elastic deformation behavior in a Ti/Mo-based alloy. *Scr Mater* 50:343–348
- [10] Maeshima T, Nishida M (2004) Shape memory properties of biomedical Ti–Mo–Ag and Ti–Mo–Sn alloys. *Mater Trans* 45:1096–1100
- [11] Zhang LC, Zhou T, Alpay SP, Aindow M, Wu MH (2005) Origin of pseudoelastic behavior in Ti–Mo-based alloys. *Appl Phys Lett* 87:241909
- [12] Kim HY, Ohmatsu Y, Kim JI, Hosoda H, Miyazaki S (2004) Mechanical properties and shape memory behavior of Ti–Mo–Ga alloys. *Mater Trans* 45:1090–1095
- [13] Kim HY, Ikehara Y, Kim JI, Hosoda H, Miyazaki S (2006) Martensitic transformation, shape memory effect and superelasticity of Ti–Nb binary alloys. *Acta Mater* 54:2419–2429
- [14] Ho WF, Ju CP, Chern Lin JH (1999) Structure and properties of cast binary Ti–Mo alloys. *Biomaterials* 20:2115–2122
- [15] Zhao X, Niinomi M, Nakai M, Hieda J (2012) Beta type Ti–Mo alloys with changeable Young’s modulus for spinal fixation applications. *Acta Biomater* 8:1990–1997
- [16] Sabeena M, Mythili R, Joysurya B, Vijayalakshmi M (2013) Thermodynamic basis of non-equilibrium phase transformations of bcc  $\beta$ -phase in Ti–Mo system. *Trans Indian Inst Metals* 66:401–407
- [17] Hanada S, Yoshio T, Izumi O (1986) Effect of plastic deformation modes on tensile properties of beta titanium alloys. *Trans Jpn Inst Metals* 27:496–503
- [18] Hanada S, Izumi O (1987) Correlation of tensile properties, deformation modes, and phase stability in commercial  $\beta$ -phase titanium alloys. *Metall Trans A* 18:265–271
- [19] Marteleur M, Sun F, Gloriant T, Vermaut P, Jacques PJ, Prima F (2012) On the design of new  $\beta$ -metastable titanium alloys with improved work hardening rate thanks to simultaneous TRIP and TWIP effects. *Scr Mater* 66:749–752
- [20] Sun F, Zhang JY, Marteleur M, Gloriant T, Vermaut P, Laille D et al (2013) Investigation of early stage deformation mechanisms in a metastable  $\beta$  titanium alloy showing combined twinning-induced plasticity and transformation-induced plasticity effects. *Acta Mater* 61:6406–6417
- [21] Karasevskaya O, Ivasishin OM, Semiatin SL, Matviychuk YV (2003) Deformation behavior of beta-titanium alloys. *Mater Sci Eng A* 354:121–132
- [22] Nakai M, Niinomi M, Oneda T (2011) Improvement in fatigue strength of biomedical  $\beta$ -type Ti–Nb–Ta–Zr alloy while maintaining low young’s modulus through optimizing  $\omega$ -phase precipitation. *Metall Mater Trans A* 43:294–302
- [23] Lin DJ, Chern Lin JH, Ju CP (2002) Structure and properties of Ti–7.5Mo–xFe alloys. *Biomaterials* 23:1723–1730
- [24] Hsiung LM, Lassila DH (2000) Shock-induced deformation twinning and omega transformation in tantalum and tantalum-tungsten alloys. *Acta Mater* 48:4851–4865
- [25] Wang YB, Zhao YH, Lian Q, Liao XZ, Valiev RZ, Ringer SP et al (2010) Grain size and reversible beta-to-omega phase transformation in a Ti alloy. *Scr Mater* 63:613–616
- [26] Yang Y, Li GP, Cheng GM, Li YL, Yang K (2009) Multiple deformation mechanisms of Ti–22.4Nb–0.73Ta–2.0Zr–1.34O alloy. *Appl Phys Lett* 94:061901
- [27] Furuta T, Kuramoto S, Rong C, Hwang J, Nishino K, Saito T et al (2006) Effect of oxygen on phase stability and elastic deformation behavior in gum metal. *J Jpn Inst Metals* 70:579–585
- [28] Sun F, Prima F, Gloriant T (2010) High-strength nanostructured Ti–12Mo alloy from ductile metastable beta state precursor. *Mater Sci Eng A* 527:4262–4269
- [29] Ping D (2014) Review on  $\omega$  phase in body-centered cubic metals and alloys. *Acta Metall Sin* 27:1–11
- [30] Ng HP, Devaraj A, Nag S, Bettles CJ, Gibson M, Fraser HL et al (2011) Phase separation and formation of omega phase in the beta matrix of a Ti–V–Cu alloy. *Acta Mater* 59:2981–2991
- [31] Qin D, Lu Y, Zhang K, Liu Q, Zhou L (2012) X-ray photoelectron spectroscopy characterization of the  $\omega$  phase in water quenched Ti–5553 alloy. *Mater Charact* 73:77–80
- [32] Prima F, Vermaut P, Texier G, Ansel D, Gloriant T (2006) Evidence of  $\alpha$ -nanophase heterogeneous nucleation from  $\omega$  particles in a  $\beta$ -metastable Ti-based alloy by high-resolution electron microscopy. *Scr Mater* 54:645–648
- [33] Devaraj A, Nag S, Srinivasan R, Williams REA, Banerjee S, Banerjee R et al (2012) Experimental evidence of concurrent compositional and structural instabilities leading to  $\omega$  precipitation in titanium-molybdenum alloys. *Acta Mater* 60:596–609
- [34] De Fontaine D, Paton NE, Williams JC (1971) The omega phase transformation in titanium alloys as an example of displacement controlled reactions. *Acta Metall Mater* 19:1153–1162
- [35] Zhao X, Niinomi M, Nakai M, Hieda J (2012) Effect of deformation-induced omega phase on the mechanical properties of metastable beta-type Ti–V alloys. *Mater Trans* 53:1379–1384
- [36] Davis R, Flower HM, West DRF (1979) Martensitic transformations in Ti–Mo alloys. *J Mater Sci* 14:712–722. doi:10.1007/BF00772735

- [37] Hanada S, Izumi O (1986) Transmission electron microscopic observations of mechanical twinning in metastable beta titanium alloys. *Metall Trans A* 17:1409–1420
- [38] Flower HM, Henry SD, West DRF (1974) The  $\beta$ - $\alpha$  transformation in dilute Ti–Mo alloys. *J Mater Sci* 9:57–64. doi:10.1007/BF00554755
- [39] Sakedai E, Shimoda M, Nishizawa H, Nako Y (2011) Nucleation behaviour of  $\beta$  to  $\omega$  phase transformations in  $\beta$ -type Ti–Mo alloys. *Mater Trans* 52:324–330
- [40] Xing H, Sun J (2008) Mechanical twinning and omega transition by  $\langle 111 \rangle \{112\}$  shear in a metastable  $\beta$  titanium alloy. *Appl Phys Lett* 93:031908
- [41] Wu SQ, Ping DH, Yamabe-Mitarai Y, Xiao WL, Yang Y, Hu QM et al (2014)  $\{112\} \langle 111 \rangle$  twinning during  $\omega$  to body-centered cubic transition. *Acta Mater* 62:122–128
- [42] Min XH, Tsuzaki K, Emura S, Tsuchiya K (2011) Enhancement of uniform elongation in high strength Ti–Mo based alloys by combination of deformation modes. *Mater Sci Eng A* 528:4569–4578
- [43] Haghghi SE, Lu HB, Jian GY, Cao GH, Habibi D, Zhang LC (2015) Effect of  $\alpha''$  martensite on the microstructure and mechanical properties of beta-type Ti–Fe–Ta alloys. *Mater Design* 76:47–54
- [44] Ren Y, Wang F, Wang S, Tan C, Yu X, Jiang J et al (2013) Mechanical response and effects of  $\beta$ -to- $\alpha''$  phase transformation on the strengthening of Ti–10V–2Fe–3Al during one-dimensional shock loading. *Mater Sci Eng A* 562:137–143
- [45] Feeney JA, Blackburn MJ (1970) Effect of microstructure on the strength, toughness, and stress-corrosion cracking susceptibility of a metastable beta titanium alloy (Ti–11.5Mo–6Zr–4.5Sn). *Metall Trans* 1:3309–3323
- [46] Min X, Tsuzaki K, Emura S, Tsuchiya K (2012) Enhanced uniform elongation by pre-straining with deformation twinning in high-strength  $\beta$ -titanium alloys with an isothermal  $\omega$ -phase. *Philos Mag Lett* 92:726–732
- [47] Zhou YL, Luo DM (2011) Microstructures and mechanical properties of Ti–Mo alloys cold-rolled and heat treated. *Mater Charact* 62:931–937